Soft Matter

Accepted Manuscript

ROYAL SOCIETY
OF CHEMISTRY

www.rsc.org/softmatter

Inducing uniform single-crystal like orientation in natural rubber with constrained uniaxial stretch

Weiming Zhou, Lingpu Meng, Jie Lu, Zhen Wang, Wenhua Zhang, Ningdong Huang, Liang Chen*, Liangbin Li[*]

National Synchrotron Radiation Lab & CAS Key Laboratory of Soft Matter Chemistry & Department of Polymer Science and Engineering, University of Science and Technology of China, Hefei, China.

Abstract: The effect of flow on crystallization is commonly attributed to entropic reduction caused by stretch and orientation of polymer chains, but overlooks the role of flow on the free energy of final state. With the aid of *in-situ* synchrotron radiation wide-angle X-ray diffraction (WAXD) and homemade constrained uniaxial tensile machine, poly-crystals possessing single-crystal like orientation rather than uniaxial orientation are found during the constrained stretch of natural rubber, whilst the *c*-axis and *a*-axis align in the stretch direction (SD) and constrained direction (CD), respectively. Molecular dynamic simulation shows that aligning a-axis of crystal nuclei in CD leads to the lowest free energy increase and favors crystal nucleation. This indicates that nomenclature of strain-induced crystallization may not fully account for the nature of flow-induced crystallization (FIC), as strain mainly emphasizes on entropic reduction of initial melt while stress rather than strain plays the dominant role in crystal deformation. Current work not only contributes to comprehensive understanding the mechanism of flow induced crystallization but also demonstrates the potential application of constrained uniaxial tensile stretch to create functional materials containing poly-crystals possessing single-crystal like orientation.

---

[*] correspondence authors: rychen@ustc.edu.cn, lbli@ustc.edu.cn

Introduction

Flow-induced crystallization (FIC) of polymer is a non-equilibrium challenge in academy and industry, as flow is inevitably involved in processing (like blowing film) as well as in service of the final products (like stretching natural rubber). [1-6] Imposing external flow can greatly enhance nucleation rate,[7-10] change crystal morphology from isotropic spherulite to oriented shish-kebab,[11, 12] and induce new crystal form,[13-16] which play an important role on the efficiency of processing and affect the properties of final products. These effects of flow on crystallization are commonly attributed to flow-induced orientation and stretch of polymer chains.[17-20] The most widely recognized mechanism for FIC is the entropic reduction model (ERM)[21-25], which has been employed to interpret flow enhanced nucleation. In ERM, the free energy of initial melt is leveled up by flow as oriented or stretched chains have lower entropy than that under quiescent condition. Under flow, the thermodynamic driving force for crystallization is expressed as $\Delta G = \Delta G_q + \Delta G_{mf}$, where ΔG_q is the thermodynamic driving force at quiescent condition. $\Delta G_{mf} = -T\Delta S_{mf}$ is the free energy change of melt induced by flow. T and ΔS_{mf} are the temperature and the entropic reduction, respectively. The physical picture of the ERM allocates the flow effect exclusively on polymer melt but overlooks the role of flow on the free energy of crystal nuclei. As FIC is a phase transition from liquid to crystal, both thermodynamics and kinetics of this phase transition are determined by the free energies of the initial melt and the final crystal state, where the latter may vary with crystal morphology[26-30] and form[31-34] as well as crystal orientation respect to flow or stress direction.[35-39]

Oriented shish nuclei[40-42] and new crystal forms[14, 43, 44] are widely reported in the study of FIC, which however have been taken into account in interpretation of FIC only recently. The transition from point to shish nuclei[40-42] and the formation of new crystal forms[31, 32] clearly demonstrate that not only the entropy of initial melt but also the enthalpy and surface free energy of final crystal nuclei are modified by flow. Thus a new term ΔG_{cf} accounting for flow-induced free energy change of crystals should be included in the thermodynamic driving force for crystallization, namely $\Delta G = \Delta G_q + \Delta G_{mf} + \Delta G_{cf}$. Recently, we observed that four types of nuclei with different morphologies and crystal forms are induced by extensional flow in lightly cross-linked high density polyethylene (XL-HDPE). Incorporating the free energies of various final states into the ERM, it is possible to explain both the enhancement of nucleation and the transition from lamellar to shish nuclei under flow.[45]

Even with the same crystal morphology and form, imposing flow (stress) can also change the free energy of crystal nuclei due to elastic deformation of lattice[46-49], which results in an increase of free energy of crystal[50] and consequently reduces thermodynamic driving force for nucleation. The free energy increased for deformed crystal can be expressed as $\Delta G_{cf} = \frac{1}{2E}\sigma^2$, here the E and σ are modulus of crystal and stress, respectively.[50] In this case, ΔG_{mf} and ΔG_{cf} act as two counter effects on nucleation, where ΔG_{mf} promotes and ΔG_{cf} postpones nucleation respectively. More interestingly, as crystal is anisotropic in structure and mechanics along different lattice directions[51-53], imposing stress with the same magnitude along different lattice directions may lead different free energies increased for crystals.

Aligning the lattice direction with the largest modulus to the stress direction is thermodynamically favorable for nucleation, as the lowest ΔG_{cf} is achieved in this case. Unfortunately, experimental evidence on differentiating lattice directions in FIC is still scarce probably due to two reasons. First, as the modulus of crystal is rather large compared to that of polymer melt[54-57], differentiating lattice directions in FIC requires relative large stress. Second, chain axis direction of polymer crystals normally has the largest modulus[51-53]. Under uniaxial shear or extension flow, chain axis direction of crystal always aligns in flow direction, which is generally attributed to flow-induced orientation of chain in melt (ΔG_{mf}) alone rather than to stress-induced free energy change of crystal (ΔG_{cf}).[56-59] Thus tiny discrimination between lattice directions by stress does occur during nucleation under uniaxial flow field, its contribution is hard to be distinguished experimentally. To solve these obstacles, imposing biaxial stress on cross-linked polymer network may be an effective approach. Here the first main stress axis aligns chain axis or *c*-axis of the crystal, and the second stress axis is employed to differentiate lattice directions in *ab* planes or (*hk0*) directions. Cross-linked polymer network is to guarantee a sufficient stress to differentiate lattice directions during FIC.

In this work, aiming to demonstrate the effect of crystal deformation on nucleation, stretch-induced crystallization of a cross-linked natural rubber is studied with *in-situ* synchrotron radiation wide angle X-ray diffraction (WAXD) measurements, during which both uniaxial free stretch (FS) and constrained stretch (CS) are imposed on, respectively. Poly-crystals possessing single-crystal like orientation rather than uniaxial orientation is observed under the CS condition, where the *c*-axis of the lattice (chain axis) aligns along the stretch direction (SD) and *a*-axis of the lattice align along the constrained direction (CD), respectively. Molecular dynamic simulation confirms that imposing constrained stress in *a*-axis or 200 direction leads to the lowest ΔG_{cf} and favors nucleation. These results show that deformation of crystal does play a role in nucleation and demonstrates a new approach to tune crystal orientation in three dimensions.

Experiment

The recipe and cure condition for preparation of the rubber sample is shown in Table 1. After being mixed with necessary ingredients, the rubber composites were compressed into a 1 mm-thick sheet by a compression molding at 143 °C and 9 min for curing. The cross-link of natural rubber was obtained through the chemical reaction of sulfur, isoprene molecule and ingredients at the curing temperature (143^{o}C). The estimated crosslinking density was 1.43×10^{-4} mol/cm^3 obtained by the nuclear magnetic resonance spectroscopy. The sheets were subsequently cut into rectangular shaped specimens for synchrotron radiation WAXD experiments. The width of sample and distance between two clamps for the rectangular specimens were 30×31 mm^2 and 18×13.5 mm^2 for uniaxial CS and FS, respectively.

Table 1. Recipes and cure conditions of vulcanized NR

ingredients	Loading level (phr^a)
natural rubber	100
stearic acid	2
ZnO	1

accelerator TT[b]	0.2
accelerator DTDM[c]	0.5
accelerator DM[d]	0.5
sulfur	1.5
curing time[e] (min)	9

[a] Parts by weight per hundred parts rubber (phr). [b] Tetramethylthiuram disulfide. [c] 4, 4′-Dithiodimorpholine. [d] N-Cyclohexyl-2-benzothiazolyl sulfenamide. [e] cure temperature was 143°C.

A home-made constrained uniaxial tensile machine[60] was used with a crosshead speed of 0.06 mm/min for stretch the NR sheets at the room temperature, during which the *in situ* synchrotron radiation WAXD was employed to record the structural evolution at the BL16B beamline in Shanghai Synchrotron Radiation Facility (SSRF). A schematic picture of the homemade uniaxial tensile device is shown in Figure 1 (a). Stretch is carried out through the two servo motor driven clamps, while scissor-like clamps in the transverse direction keeping the sample width constant. Figure 1 (b) and (c) are the schematic illustrations for CS and FS process, respectively. For CS process, the width of rubber sheet keeps constant along the CD, while the width of rubber sheet decreases in FS process. During the stretch process, the draw ratio is defined as the ratio between the length during stretch and original length, that is the draw ratio $DR = L/L_0 = (\mathrm{L}_0 + vt)/L_0 = 1 + vt/L_0$. Here the v is the stretch speed, t is the stretch time and L_0 is the original length for natural rubber sheet. Meanwhile, a mini-rotatable constrained tensile device is used to acquire the 2D-WAXD patterns at different rotation angle ψ and the schematic of the geometry for rotation of sample along the SD and WAXD measurements is presented in Figure 2 (a). Figure 2 (b) is the schematic of crystal for natural rubber induced by stretch has a space group of P21/a with lattice constants a=1.246 nm, b=0.889 nm, c=0.81 nm, α=γ=90° and β=92°.

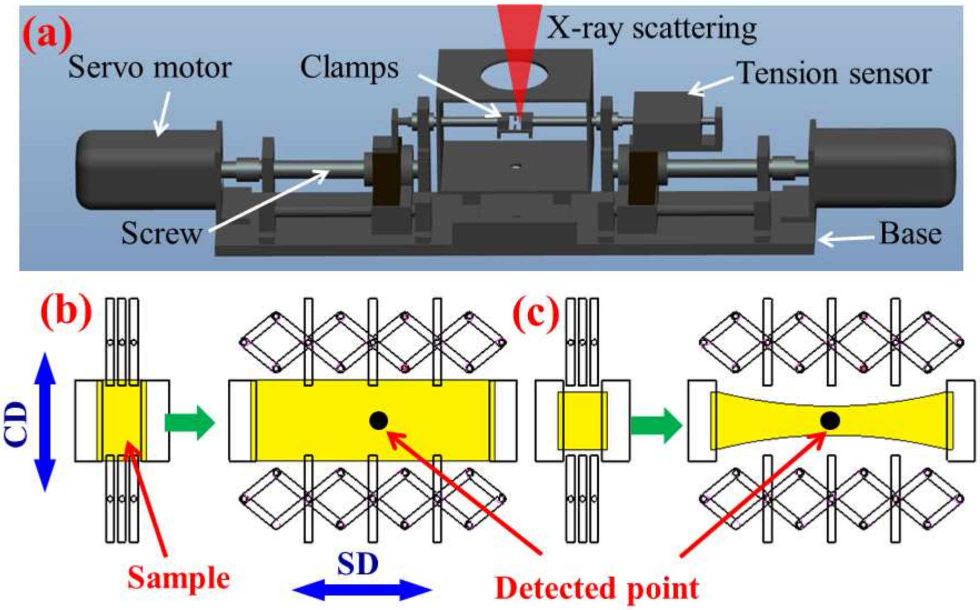

Figure 1. (a) Three-dimensional view of homemade uniaxial tensile device. Schematic of the uniaxial CS (b) and FS (c) process, respectively. The yellow pieces depict natural rubber sheets and the black circles in the middle of sample represent the detected point. The SD and CD are along the horizontal and vertical directions, respectively.

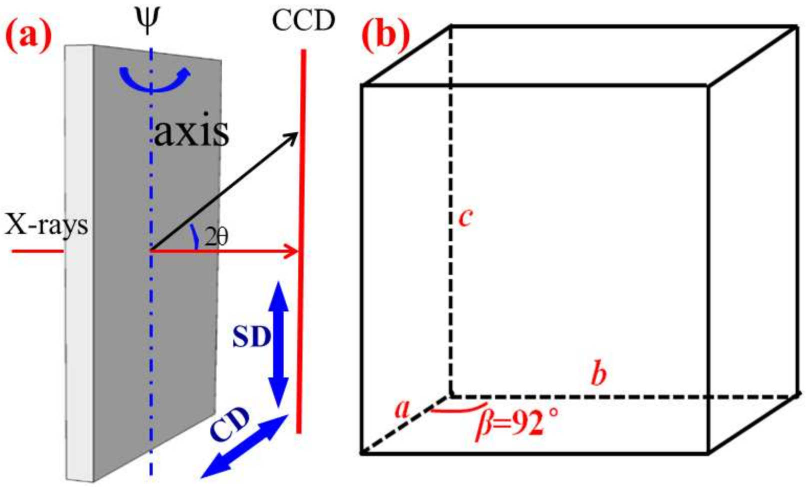

Figure 2. Schematic of the geometry for rotation of sample and WAXD measurements (a) and the crystal lattice for natural rubber (b). The incident angle between sample and X-rays can be changed through rotating the sample around the rotation axis labeled by blue dotted line. Before rotation, the incident direction of X-rays is perpendicular to the plane of mini-rotatable constrained tensile device, namely the rotation angle ψ=0°. The rotation axis can be along SD or CD, as indicated by the blue double-headed arrow. In order to implement the rotation into the configuration of the WAXS measurements, another apparatus is used with vertical SD distinctive

from those in Figure 1(b) and (c).

The X-ray energy used was 10 keV and a Mar165 CCD detector (2048×2048 pixels with pixel size of 80 μm) was employed to collect time-resolved two-dimensional (2D) WAXD patterns. The exposure time was 15 s with an additional 5 s for reading data and cleaning the memory data (i.e., patterns were acquired at a rate of 20 s/frame), thus we can obtain enough data to analyze the structure evolution during the stretching process. The sample-to-detector distance was calibrated to be 194.7 mm by Yttrium(III)-oxide (Y_2O_3) for WAXD. Fit2D software from European Synchrotron Radiation Facility (ESRF) was used to analyze the WAXD data, which was corrected for background scattering through subtracting contributions from the home-made constraint uniaxial tensile machine and air. In order to achieve the consistency, reproducibility and uniformity of the X-ray results, the middle of the sample is chosen for the detected point, which is the homogeneous deformation area of the sample during the CS and FS. The 2D WAXD patterns were integrated to obtain one-dimensional (1D) diffraction profile as a function of $2d\sin\theta=n\lambda$, d is the interplanar spacing, n is the positive integer, 2θ is the scattering angle and λ is the X-ray wavelength. The calculation of crystallinity index (CI) is described as the following equation:

$$\mathrm{CI}=\frac{\sum_{crystal} 2\pi\int \sin\phi d\phi \int I(\mathrm{s})\,\mathrm{s}^2\, ds}{\sum_{total} 2\pi\int \sin\phi d\phi \int I(\mathrm{s})\,\mathrm{s}^2\, ds} \quad , \tag{1}$$

where I(s) represents the intensity distribution of each peak that is read out from the WAXD pattern, s is the radical coordinate in reciprocal space in nm^{-1} unit ($s=2\sin\theta/\lambda$, where λ is the wavelength and 2θ is the scattering angle), and ϕ is the angle between the scattering vector of the peak and the stretching direction.

The total energies of the crystals for natural rubber at different draw ratios were obtained with the help of Geometry Optimization task, Forcite module in Materials Studio 6.0 software (Accelrys Inc.). The polymer consistent forcefield (PCFF), smart algorithm and ultra-fine quality were used for Geometry Optimization in all the simulations. Supercell (3×3×3) with 216 segments of isoprene and iteration of 10000 were used in order to improve the precision of the simulation results.

Results and discussion

Figure 3 presents the engineering stress-draw ratio curves during CS and FS. Under the same draw ratio, the engineering stress for CS is larger than that for FS, while the elongation at break for CS is smaller than that for FS. Under CS condition as the width keeps constant, the deformation mainly takes place in thickness. Larger stress under CS condition is partly due to the counterforce imposed by the scissor-like clamps in the CD and consequently induce larger entropy reduction compared with that under FS condition for the same draw ratio.[61]

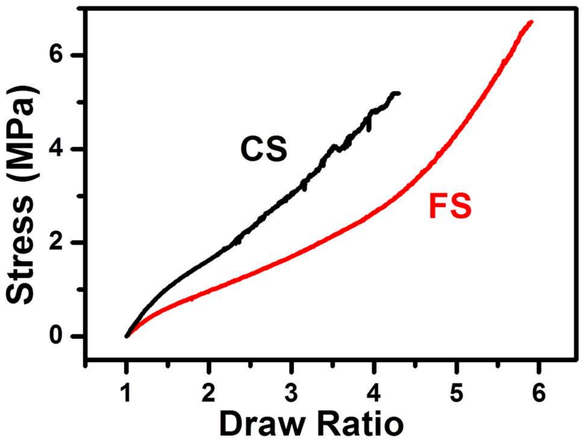

Figure 3. The engineering stress-draw ratio curves for CS and FS.

The selected 2D WAXD patterns at different draw ratios under CS and FS conditions are presented in Figure 4. Crystal diffractions of natural rubber appear as draw ratio reaches about 2.65 under CS, which is smaller than that about 2.85 under FS. This indicates constraint in CD induce a relative larger entropy reduction, although it is perpendicular to the SD and the chain orientation of crystals. The 200, 201, 120 and 002 diffraction planes of nature rubber crystals can be easily found in Figure 3 as labeled in words with white color, indicating that crystals align their chain parallel to SD under both CS and FS conditions. Meanwhile, during the period of stretch, the nuclei rapidly formed at high strain and allowing no time for filament growth, so the morphology of crystals is consists of chains of nuclei (γ-filaments) aligned with the stretching direction[41], causing the 002 diffractions plane parallel to the SD under CS and FS. The stark difference between CS and FS is the relative intensity between different diffraction planes. Under FS condition, the intensity of 120 plane is obviously stronger than that of 200 plane, while the opposite is observed under CS condition. This strong contrast suggests crystals of natural rubber induced by CS may differ from those formed under FS condition in terms of shape or orientation, as will be analyzed with details in the following.

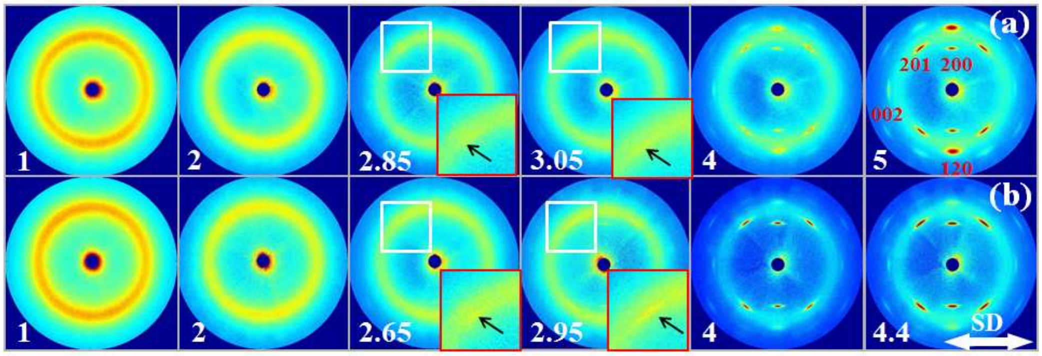

Figure 4. Selected *in-situ* 2D WAXD patterns for natural rubber under the FS (a) and CS (b). The white numbers in the left bottom corner of each pattern represent experimental draw ratio and the 200, 201, 120 and 002 planes can be found in the 2D diffraction as labeled in words with white color. The SD is horizontal, as indicated by the white double-headed arrow. The crystal diffraction signals of natural rubber appear at the draw ratio of 2.85 and 2.65 for FS and CS, respectively. To make the diffraction signal at the low draw ratio more obvious (middle four patterns), the 201 diffraction planes (inside the white rectangle block) are zoomed in as displayed in the down right corner and are indicated by the black arrows

Figures 5 (a) and (b) plot 1D diffraction profiles integrated from the 2D WAXD patterns for FS and CS, respectively. To highlight and increase the relative signal intensity of the 120 and 200 diffraction planes, the integration only covers a small azimuthal angle range in equatorial direction as shown in the insertion of Figure 5 (b), as crystals are highly oriented and both 120 and 200 diffraction planes locate in this azimuthal angle range. Under FS condition, strong diffraction intensities are perceived for both diffraction planes give strong diffraction intensities. While under CS, only 200 diffraction plane remains strong and 120 diffraction plane is rather weak, confirming the observation from the 2D WAXD patterns shown in Figure 3.

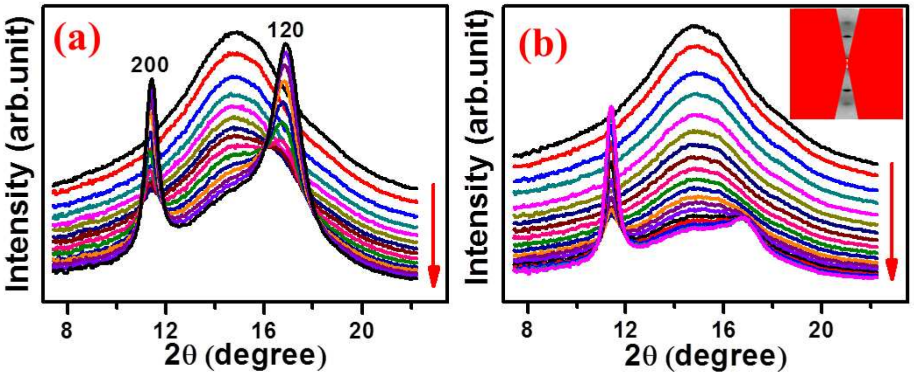

Figure 5. One-dimensional WAXD intensity curves of natural rubber during the FS (a) and CS (b) process. 2D WAXD pattern in upper right corner shows the mask protocol used for integration.

A quantitative analysis of intensity ratio (I_{120}/I_{200}) between 120 and 200 diffraction planes is presented in Figure 6 (a). The intensity ratio (I_{120}/I_{200}) for FS is about 0.21 at the onset of crystallization and increases with draw ratio, approaching 2.0 before break. Whilst under CS condition, the intensity ratio (I_{120}/I_{200}) is negligibly small (close to 0) at the appearance of crystal and reaches 0.26 before break. The intensity ratio (I_{120}/I_{200}) under FS condition is close to one order larger than that under CS for the same draw ratio. The low intensity of 120 diffraction plane measured under CS condition is probably caused by the peculiar orientation of natural rubber crystals induced by CS as other possibilities will be ruled out as follows. Figure 6 (b) shows crystallinity evolution during the FS and CS process. During the stretch process, the short chains between cross-links will first be stretched to the critical strain and induce crystallization. With the draw ratio increase, the long chains between cross-link will be subsequently increased to the critical strain and crystallize[62, 63], causing the increase in crystallinity. As mentioned earlier, under CS condition crystallization occurs at smaller draw ratio than that under FS. Meanwhile, the overall crystallinity under CS is still larger than that under FS condition at the same draw ratio. This indicates that constraint in CD plays a role on the increase of crystallinity. Note the crystallinity under CS may be underestimated due to possible orientation of 120 plane. Nevertheless even with possible underestimation the crystallinity under CS is still higher than FS under the same draw ratio, which excludes the role of crystallinity on the low diffraction intensity of 120 plane. Figures 6 (c) and (d) depict the crystal sizes in 200 and 120 directions, respectively, which are calculated with Scherrer equation based on the full width at half maximum (FWHM) of the corresponding diffraction peaks.[64] Here the crystal sizes along 200 and 120 directions show decreasing trend as the draw ratio increase, similar to the previous results.[65] Meanwhile, the crystal sizes in both 200 and 120 directions under CS are larger than those under FS, but the ratios between these two directions is comparable (around 1), indicating the aspect ratios of crystals induced by CS and FS are similar. Thus the low intensity ratio I_{120}/I_{200} under CS is not due to crystal size or aspect ratio.

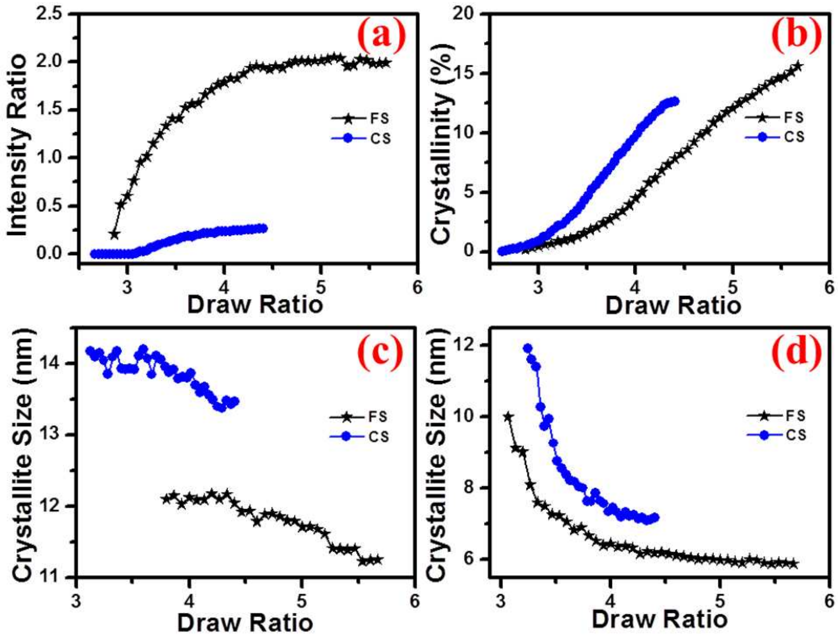

Figure 6. The intensity ratio of I_{120}/I_{200} (a), crystallinity (b), crystallite sizes along the 200 (c) and 120 (d) directions for different draw ratios under CS and FS.

After excluding other possible origins like crystallinity and crystal aspect ratio, crystal orientation will be inspected as the most plausible cause for the low intensity ratio of I_{120}/I_{200} under CS, we are going to check the crystal orientation. The 2D WAXD patterns shown in Figure 4 reveal that chain axis or *c*-axis of crystal aligns parallel to SD under both stretch conditions. With the geometry illustrated in Figure 2(a), we take 2D WAXD measurements on CS sample at drawing ratio of 4 through a ψ scanning with SD or CD as the rotation axis. During the experiment of obtaining diffraction signal at the different rotation angle, the SD is vertical direction. Thus we shifted the patterns 90 degrees to make the diffraction patterns similar to that presented in the Figure 3 for easier understanding. After subtract the amorphous and background diffraction signal with the method described in the previous paper,[17, 66] the 2D crystal diffraction patterns collected at different ψ positions with the rotation axis are the SD or CD are obtained and presented in Figure 7 (a) and (b), respectively. At $\psi=0^{o}$, the intensity of 120 diffraction plane is weak, similar to the above mentioned results in Figure 3. Rotating ψ away from 0^{o} with the rotation axis is SD, the diffraction intensity of 200 plane decreases, while that of 120 plane increases. However, the intensity of 200 diffraction plane seems very strong with the rotation angle ψ increasing when the rotation axis is CD. Based on the Figure 7 (a) and (b), a conclusion can be obtained that is the *a*-axis of the natural rubber crystal should be along the CD. The quantitative intensity ratio of I_{120}/I_{200} at different ψ as the rotation axis is SD is plotted in Figure 7 (c), which shows a continuous increase up to the maximum measurable ψ angle of 72.5^{o} on our CS setup. This suggests that the *ab* planes or (*hk0*) directions of crystals prefer orientations with 120 away from while 200 nearly parallel to the CD, respectively. To eliminate the influence of sample thickness, we plot the diffraction intensity ratio of $I_{200}/I_{amorphous}$ and $I_{120}/I_{amorphous}$ versus ψ in Figure 7 (d). The $I_{200}/I_{amorphous}$ curve shows a maximum at about 10°, which suggests that *a*-axis of crystal parallel with the CD as natural rubber crystal has a monoclinic unit cell with $\beta=92^{o}$.[67] Thus natural rubber crystals induced by CS show a single crystal-like orientation with *c*-axis and *a*-axis aligning in SD and CD, respectively, though the crystals are polycrystals. For the convenience to view the orientations of crystal lattice planes related to SD and CD, a schematic of crystal lattice is presented in Figure 8.

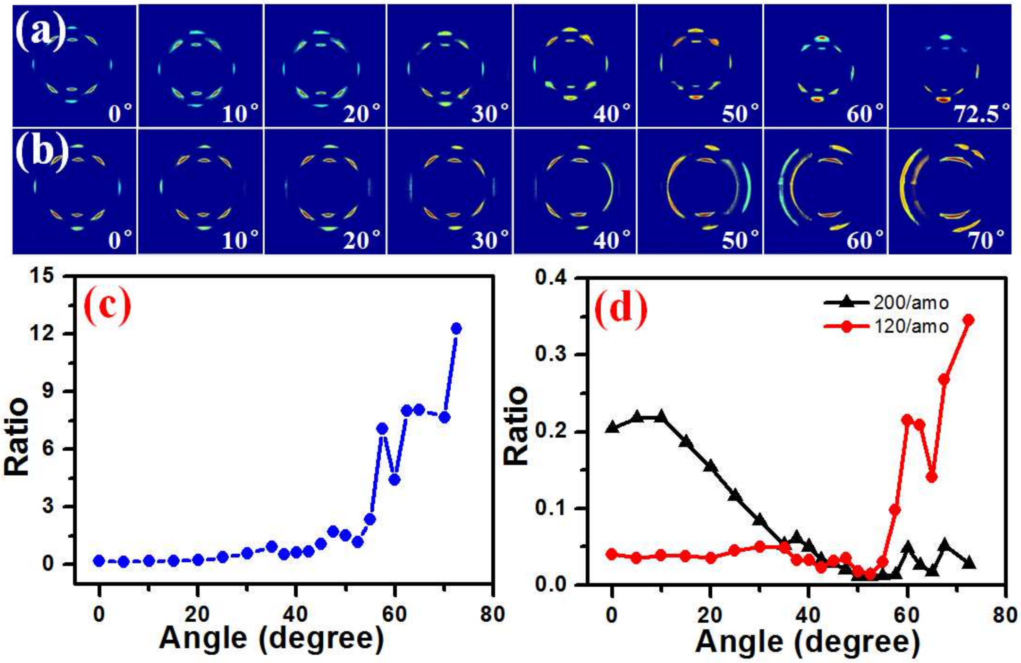

Figure 7. The 2D crystals diffraction patterns for different rotation angles as the rotation axis are the SD (a) and CD (b), the words with the white color in the right bottom corner of each pattern represent the rotation angle, (c) the relation between diffraction intensity ratio of I_{120}/I_{200} versus rotation angle ψ as the rotation angle is SD, (d) the ratio of relative diffraction intensity of $I_{120}/I_{amorphous}$ and $I_{200}/I_{amorphous}$ versus rotation angle ψ as the rotation angle is SD.

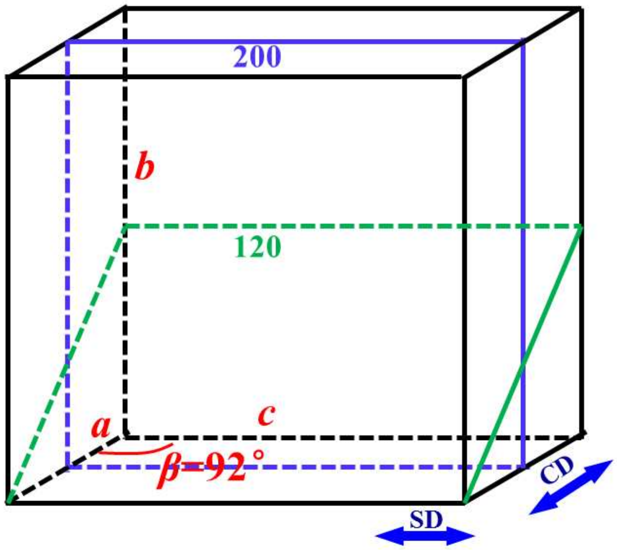

Figure 8. The schematic of crystal lattice for natural rubber generated under the CS condition. The crystal of natural rubber has a space group of P21/a with lattice constants a=1.246 nm, b=0.889nm,c=0.81 nm, α=γ=90° and β=92°. 200 and 120 planes are specified with blue and green

lines, respectively.

What determine the transition from uniaxial orientation to single-crystal like orientation under CS? As polymer chains in the amorphous state are already pre-aligned parallel to SD, it is a natural consequence for *c*-axis of crystal aligning in SD. On the other hand, aligning *a*-axis in CD is a selection among all (*hk0*) lattice planes. We attribute the selection of lattice orientation to thermodynamics of nucleation under CS condition. Figure 9 (a) depicts the free energy landscapes of crystallization at quiescent and under strain within the framework of the ERM. As mentioned in the introduction, the ERM attributes external work from flow to polymer melt only while assumes the same free energy of crystal as that at quiescent condition, which leads to a lower nucleation barrier and a higher nucleation rate. Our recent work indicates that the assumption of unchanged crystal free energy is invalid and demonstrates sensitivity to the morphology and structure of crystal nuclei[61]. In current work, the morphology and structure of nuclei under CS condition may be the same as that at quiescent, but different orientations of crystal nuclei respect to CD can induce different free energy changes ΔG_{cf}. As stress increases free energy of crystal, aligning a lattice direction with the least free energy increase will achieve the fast nucleation rate. Thus an intuitive picture is that the lattice direction of crystal with the highest modulus lays aligns in SD, while the second high modulus lattice direction aligns in CD. Based on the previous results, the moduli along *a*-, *b*- and *c*-axis directions are 9.04, 8.44 and 13.3 GPa, respectively.[51] This modulus qualitatively confirms the idea of differentiating lattice directions during crystal nucleation.

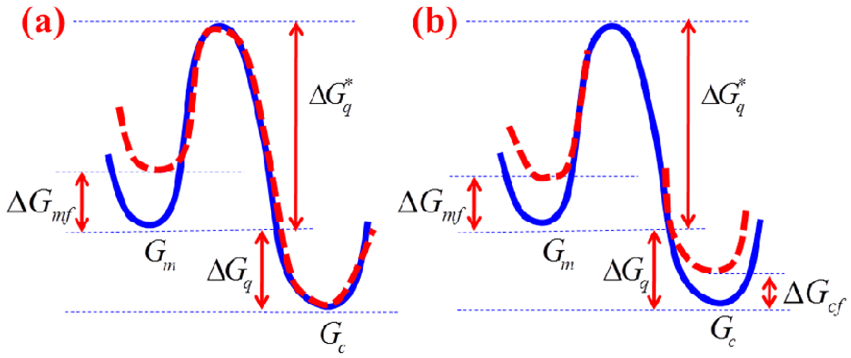

Figure 9. Schematic illustration of the free energy changed induced by stretch (red dashed curve) in comparison to that at quiescent condition (solid blue curve) as a function of degree of order. (a) The classical ERM only involves the effect of the strain on entropic reduction of melt only without changing the free energy of final crystal. (b) The modified ERM considers the orientation of crystal nuclei respect to CD in the final stage of nucleation as well. G is the free energy of certain state, where the subscript m and c represent melt and crystal, respectively. ΔG_q is fundamental thermodynamic driving force in quiescent condition. ΔG_q^* is the nucleation barrier of critical nuclei. ΔG_{mf} is free energy change of melt state induced by flow. ΔG_{cf} is the free energy increased by orientation of crystal nuclei.

For quantitative analysis, we employ molecular dynamic simulation to calculate the free energy change ΔG_{cf} of crystal with *a*- and *b*-axis aligning in CD, respectively. The interplanar crystal spacing for 200, 120 and 002 planes can be obtained through the Braggs law with the peak positions. Figure 10 (a) depicts the strains for crystal lattice along *a*-, *b*-, *c*-axis directions at different macroscopic draw ratios, where the lattice constants at quiescent condition is used as the references. The lattice parameters at both CS and FS conditions are larger than their values at quiescent condition at the draw ratio of 3.3, similar to previous results[46, 48]. Increasing the draw ratio, the lattice strains along *a*- and *b*-axis decrease while *c*-axis increases under both CS and FS conditions. Meanwhile, imposing constraint in CD, the deformation of crystal under CS is significantly reduced. At draw ratio of 3.3, the strains along *a*-, *b*- and *c*-axis are about of 0.29%, 0.73% and 0.99% under CS condition in comparison to 1.02%, 0.80% and 1.61% under FS condition, respectively. Lower strain corresponds to lower ΔG_{cf}, which partly contributes to the lower draw ratio to induce crystallization under CS than that under FS.

As mentioned in introduction, crystallization is driven by $\Delta G = \Delta G_q + \Delta G_{mf} + \Delta G_{cf}$. Assuming the same ΔG, smaller deformation of crystal means a smaller ΔG_{cf}, which correspondingly requires a smaller $\Delta G_{mf} = -T\Delta S_{mf}$ or draw ratio α to compensate as $\Delta S_{mf} = -\nu k(\alpha^2 + 2/\alpha - 3)/2$. Here ν, α and k are crosslink density, draw ratio and Boltzmann constant, respectively.[68] To verify that aligning *a*-axis rather than *b*-axis in CD has a lower ΔG_{cf} under CS condition, we calculate ΔG_{cf} through the molecular dynamic simulation as plotted in Figure 10 (b). The lattice parameters used for molecular dynamic when aligning *a*-axis in CD are derived from the experimental results, namely a_{a-axis}, b_{a-axis} and c_{a-axis}, where the subscript *a-axis* means *a*-axis aligns in CD direction. Whilst aligning *b*-axis in CD, the lattice parameters are defined as $a_{b\text{-}axis} = a_0[\frac{E_b}{E_a}(\frac{b_{a-axis}}{b_0} - 1) + 1]$, $b_{b\text{-}axis} = b_0[\frac{E_a}{E_b}(\frac{a_{a-axis}}{a_0} - 1) + 1]$ and $c_{b\text{-}axis} = c_{\text{a-}axis}$, assuming that the same stress is uploaded on the crystal lattice. Here a_0 and b_0 are the lattice parameters along the *a*-axis and *b*-axis directions at quiescent condition, respectively. E_a and E_b are the moduli for the crystal along *a*- and *b*-axis directions, respectively. Form Figure 10 (b), the ΔG_{cf} for CD along *b*-axis is about 0.086 kJ/mol larger than that along *a*-axis at the draw ratio of 3.3, indicating that a lower ΔG_{cf} favoring for nucleation is achieved with CD along *a*-axis. Based on the ERM model, the ΔS_{mf} can be expressed as $\Delta S_{mf} = \Delta H(\frac{1}{T_m(\alpha_i)} - \frac{1}{T_m(1)})$, taking the $\Delta H = 13.92$ kJ/mol, $T_m(1) = 256$ K, $T_m(\alpha_i) = 298$ K[22], thus $\Delta G_{mf} = -T_m(\alpha_i)\Delta S_{mf} = 2.283$ kJ/mol can be obtained. The calculated ΔG_{cf} difference between crystal aligning *a*- and *b*-axes in CD is only about 3.77% of ΔG_{mf}, but it is sufficient for crystal nuclei to differentiate their favorable orientation. This quantitatively explains the preferential orientation of 200 in CD and provides a direct evidence for differentiating lattice direction during stretch or flow-induced crystallization.

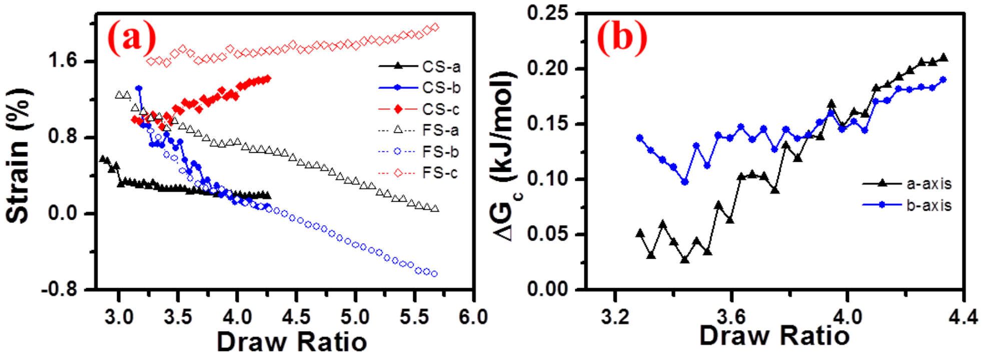

Figure 10. (a) The lattice strain along *a*-, *b*- and *c*-axis for CS and FS conditions, (b) the relation between the total free energy increased for polymer segment in the lattice and draw ratio for CS when the CD are along *a*-axis and *b*-axis.

The above experimental results and analysis clearly demonstrate the importance to incorporate the free energy of final crystal in FIC. As mentioned in introduction, the thermodynamic driving force for crystallization can be written as $\Delta G = \Delta G_q + \Delta G_{mf} + \Delta G_{cf}$. The classical ERM only consider ΔG_{mf} due to flow-induced chain stretch and orientation, which can be estimated with the theory for rubber elasticity[61] or theory for polymer dynamics like Doi-Edwards model[69]. Here we include a new term ΔG_{cf} to describe the change of free energy of crystals by stretch and analyze several possible origins for ΔG_{cf} as follows. Different morphologies like folded-chain, fringe-micellar and shish nuclei induced by flow will contribute different surface free energies on nucleation barrier, while different crystal forms will have different bulk free energies. Even with the same crystal form and morphology, stress-induced deformation of crystal will level up the energy of crystal, which introduces extra penalty on crystallization. All these factors influence crystallization kinetics such as nucleation rate. Whilst due to intrinsically anisotropic nature of crystal, the same stress on different lattice directions results in different free energy change. External stress can differentiate lattice direction during nucleation and induce peculiar orientation of crystal. Following this line, the nomenclature of strain-induced crystallization may not fully account the nature of FIC, as strain mainly emphasizes entropic reduction ΔG_{mf} of initial melt while stress rather than strain plays the dominant role in crystal deformation.

The single-crystal like orientation induced by CS gives an indication on tuning crystal in three dimensions. If the orientations of both *a*- and *c*-axis are fixed, *b*-axis is also defined. This means polycrystalline sample can be aligned into a single-crystal like pattern, which may show peculiar mechanical, electro-optical and other properties. Thus current finding suggests that CS is an effective approach to create functional materials containing uniform aligned polycrystals.

Conclusions

In-situ WAXD measurements reveal that single-crystal like orientation of natural rubber polycrystals are induced by constrained uniaxial tensile stretch, where *c*- and *a*-axis align in SD and CD, respectively. Incorporating the free energy change ΔG_{cf} of crystal nuclei induced by external stress, this peculiar orientation of crystal is interpreted. Molecular dynamic simulation shows that a lower ΔG_{cf} is achieved with CD imposing along *a*-axis, which is favorable for nucleation. Our results and analysis reveal that the nomenclature of strain-induced crystallization may not fully account the nature of FIC, the free energy of final state induced by flow should also be incorporate into the thermodynamic driving force for crystallization.

Acknowledgement

The authors would like to thank Prof. Luyuan Hao (University of Science and Technology of China, Hefei, China) and Mr. Teng Zhang (University of Notre Dame, Notre Dame, United States) for their kindly help on the discussion and calculation of the molecular dynamic simulation. This work is supported by National Natural Science Foundation of China (51473151, 51325301, 51120135002), the Project 2013BB05 supported by NPL, CAEP. The experiment is partially carried out in National Synchrotron Radiation Lab (NSRL) and BL16B beamline of Shanghai Synchrotron Radiation Facility (SSRF).

References

1. J. M. Schultz, B. S. Hsiao and J. M. Samon, *Polymer*, 2000, **41**, 8887-8895.
2. M. van Drongelen, D. Cavallo, L. Balzano, G. Portale, I. Vittorias, W. Bras, G. C. Alfonso and G. W. M. Peters, *Macromol. Mater. Eng.*, 2014, **299**, 1494-1512.
3. M. Zhang, L. Zha, H. Gao, Y. Nie and W. Hu, *Chin. J. Polym. Sci.* , 2014, **32**, 1218-1223.
4. W. Zhou, X. Li, J. Lu, N. Huang, L. Chen, Z. Qi, L. Li and H. Liang, *Sci. Rep.*, 2014, **4**, 7502.
5. J. Carretero-Gonzalez, T. A. Ezquerra, S. Amnuaypornsri, S. Toki, R. Verdejo, A. Sanz, J. Sakdapipanich, B. S. Hsiao and M. A. Lopez-Manchado, *Soft Matter*, 2010, **6**, 3636-3642.
6. J. Liu, S. Wu, Z. Tang, T. Lin, B. Guo and G. Huang, *Soft Matter*, 2015.
7. F. Yu, H. Zhang, Z. Wang, W. Yu and C. Zhou, *Chin. J. Polym. Sci.* , 2010, **28**, 657-666.
8. Z. Ma, L. Balzano, T. van Erp, G. Portale and G. W. M. Peters, *Macromolecules*, 2013, **46**, 9249-9258.
9. F. Su, W. Zhou, X. Li, Y. Ji, K. Cui, Z. Qi and L. Li, *Macromolecules*, 2014, **47**, 4408-4416.
10. Y. Hayashi, G. Matsuba, Y. F. Zhao, K. Nishida and T. Kanaya, *Polymer*, 2009, **50**, 2095-2103.
11. N. Tian, D. Liu, X. Li, Z. Wang, S. Zhu, K. Cui, W. Zhou and L. Li, *Soft Matter*, 2013.
12. B. Shen, Y. R. Liang, J. A. Kornfield and C. C. Han, *Macromolecules*, 2013, **46**, 1528-1542.
13. K. Tashiro, S. Sasaki and M. Kobayashi, *Macromolecules*, 1996, **29**, 7460-7469.
14. R. H. Somani, B. S. Hsiao, A. Nogales, H. Fruitwala, S. Srinivas and A. H. Tsou, *Macromolecules*, 2001, **34**, 5902-5909.
15. B. Luo, H. Li, Y. Zhang, F. Xue, P. Guan, J. Zhao, C. Zhou, W. Zhang, J. Li, H. Huo, D. Shi, D. Yu and S. Jiang, *Ind. Eng. Chem. Res.*, 2014, **53**, 13513-13521.
16. D. W. Schaefer, J. Zhao, H. Dowty, M. Alexander and E. B. Orler, *Soft Matter*, 2008, **4**, 2071-2079.
17. M. Tosaka, K. Senoo, S. Kohjiya and Y. Ikeda, *J. Appl. Phys.*, 2007, **101**, 084909.
18. N. Tian, W. Zhou, K. Cui, Y. Liu, Y. Fang, X. Wang, L. Liu and L. Li, *Macromolecules*, 2011, **44**, 7704-7712.
19. T. Yan, B. Zhao, Y. Cong, Y. Fang, S. Cheng, L. Li, G. Pan, Z. Wang, X. Li and F. Bian, *Macromolecules*, 2009, **43**, 602-605.
20. Y. Nie, H. Gao, Y. Wu and W. Hu, *Soft matter*, 2013, **10**, 343-347.
21. P. J. Flory, *J. Chem. Phys.*, 1947, **15**, 397-408.
22. T. G. Fox, P. J. Flory and R. E. Marshall, *J. Chem. Phys.*, 1949, **17**, 704-706.
23. G. S. Y. Yeh, *Polym. Eng. Sci.*, 1976, **16**, 138-144.
24. G. S. Y. Yeh and K. Z. Hong, *Polym. Eng. Sci.*, 1979, **19**, 395-400.
25. M. Yamamoto and J. L. White, *J. Polym. Sci. Part A-2: Polym. Phys.* , 1971, **9**, 1399-1415.
26. E. L. Heeley, C. M. Fernyhough, R. S. Graham, P. D. Olmsted, N. J. Inkson, J. Embery, D. J. Groves, T. C. B. McLeish, A. C. Morgovan, F. Meneau, W. Bras and A. J. Ryan, *Macromolecules*, 2006, **39**, 5058-5071.
27. G. Kumaraswamy, A. M. Issaian and J. A. Kornfield, *Macromolecules*, 1999, **32**, 7537-7547.
28. G. Kumaraswamy, J. A. Kornfield, F. Yeh and B. S. Hsiao, *Macromolecules*, 2002, **35**, 1762-1769.
29. G. Matsuba, C. Ito, Y. F. Zhao, R. Inoue, K. Nishida and T. Kanaya, *Polym. J.*, 2013, **45**, 293-299.
30. Y. Yang, J. T. Xu, B. Y. Du, L. Xue, Z. Q. Fan, S. M. Mai and A. J. Ryan, *J. Chem. Phys.*,

2008, **128**, 154902.

31. H. Uehara, T. Kanamoto, A. Kawaguchi and S. Murakami, *Macromolecules*, 1996, **29**, 1540-1547.
32. X. Sun, H. Li, J. Wang and S. Yan, *Macromolecules*, 2006, **39**, 8720-8726.
33. M. Zhou, S. M. Xu, Y. H. Li, C. He, T. X. Jin, K. Wang, H. Deng, Q. Zhang, F. Chen and Q. Fu, *Polymer*, 2014, **55**, 3045-3053.
34. M. Sharma, G. Madras and S. Bose, *Phys Chem Chem Phys*, 2014, **16**, 16492-16501.
35. U. C. Oh and J. H. Je, *J. Appl. Phys.*, 1993, **74**, 1692-1696.
36. K. Tashiro, M. Kobayashi and H. Tadokoro, *Macromolecules*, 1977, **10**, 413-420.
37. A. Keller, *Philos. Mag.*, 1957, **2**, 1171-1175.
38. S. H. Paek, *J. Ind. Eng. Chem.*, 2001, **7**, 316-325.
39. J. Mukherjee and A. N. Beris, *J. Comput. Theor. Nanos.*, 2010, **7**, 726-737.
40. F. Azzurri and G. C. Alfonso, *Macromolecules*, 2005, **38**, 1723-1728.
41. E. H. Andrews, *Proc. R. Soc. Lond. A-Math. Phys. Sci.*, 1964, **277**, 562-570.
42. M. D'Haese, O. O. Mykhaylyk and P. Van Puyvelde, *Macromolecules*, 2011, **44**, 1783-1787.
43. T. Yamamoto, *J Macromol Sci Phys*, 1979, **16**, 487-509.
44. H. Liu and H. Huo, *Colloid Polym Sci*, 2013, **291**, 1913-1925.
45. D. Liu, N. Tian, N. Huang, K. Cui, Z. Wang, T. Hu, H. Yang, X. Li and L. Li, *Macromolecules*, 2014, **47**, 6813-6823.
46. M. Tosaka, S. Murakami, S. Poompradub, S. Kohjiya, Y. Ikeda, S. Toki, I. Sics and B. S. Hsiao, *Macromolecules*, 2004, **37**, 3299-3309.
47. S. Poompradub, M. Tosaka, S. Kohjiya, Y. Ikeda, S. Toki, I. Sics and B. S. Hsiao, *J. Appl. Phys.*, 2005, **97**, 103529.
48. S. Kohjiya, M. Tosaka, M. Furutani, Y. Ikeda, S. Toki and B. S. Hsiao, *Polymer*, 2007, **48**, 3801-3808.
49. J. Mukherjee, S. Wilson and A. N. Beris, *J. Non-Newtonian Fluid Mech.* , 2004, **120**, 225-240.
50. S. K. F. Ansel C. Ugural, Prentice Hall PTR, Upper Saddle River, New Jersey, 1995, ch. 77-81.
51. N. Rahman, A. Isanasari, R. Anggraeni, S. Honggokusumo, M. Iguchi, T. Masuko and K. Tashiro, *Polymer*, 2003, **44**, 283-288.
52. P. Li, L. Hu, A. J. H. McGaughey and S. Shen, *Adv. Mater.* , 2014, **26**, 1065-1070.
53. R. Martoňák, W. Paul and K. Binder, *J. Chem. Phys.*, 1997, **106**, 8918-8930.
54. N. V. Pogodina, V. P. Lavrenko, S. Srinivas and H. H. Winter, *Polymer*, 2001, **42**, 9031-9043.
55. H. S. Myung, W. J. Yoon, E. S. Yoo, B. C. Kim and S. S. Im, *J. Appl. Polym. Sci.*, 2001, **80**, 2640-2646.
56. Y. Zhong, H. Fang, Y. Zhang, Z. Wang, J. Yang and Z. Wang, *ACS Sustainable Chem. Eng.*, 2013, **1**, 663-672.
57. H. Fang, Y. Zhang, J. Bai and Z. Wang, *Macromolecules*, 2013, **46**, 6555-6565.
58. Z. Ma, L. Fernandez-Ballester, D. Cavallo, T. Gough and G. W. M. Peters, *Macromolecules*, 2013, **46**, 2671-2680.
59. C. Deng, T. Fujiwara, I. Polec, G. Matsuba, L. Jin, R. Inoue, K. Nishida and T. Kanaya, *Macromolecules*, 2012, **45**, 4630-4637.
60. L. Meng, J. Li, K. Cui, X. Chen, Y. Lin, J. Xu and L. Li, *Rev. Sci. Instrum.*, 2013, **84**, 115104.
61. L. R. G. Treloar, Oxford University Press, Oxford, 2005, ch. 28-32.

62. M. Tosaka, *Macromolecules*, 2009, **42**, 6166-6174.
63. Y. Ikeda, N. Higashitani, K. Hijikata, Y. Kokubo, Y. Morita, M. Shibayama, N. Osaka, T. Suzuki, H. Endo and S. Kohjiya, *Macromolecules*, 2009, **42**, 2741-2748.
64. P. Scherrer, *Nachr. Ges. Wiss. Göttingen*, 1918, **2**, 96-100.
65. Y. Ikeda, Y. Yasuda, K. Hijikata, M. Tosaka and S. Kohjiya, *Macromolecules*, 2008, **41**, 5876-5884.
66. S. Toki, I. Sics, S. F. Ran, L. Z. Liu, B. S. Hsiao, S. Murakami, K. Senoo and S. Kohjiya, *Macromolecules*, 2002, **35**, 6578-6584.
67. C. W. Bunn, *Proc. R. Soc. Lond. A*, 1942, **180**, 0040-0066.
68. W. R. Krigbaum and R. J. Roe, *J. Polym. Sci., Part A: Polym. Chem.* , 1964, **2**, 4391-4414.
69. S. F. E. M. Doi, Clarendon Press, Oxford, 1988.

for the Table of contents entry

Inducing uniform single-crystal like orientation in natural rubber with constrained uniaxial stretch

Weiming Zhou, Lingpu Meng, Jie Lu, Zhen Wang, Wenhua Zhang, Ningdong Huang, Liang Chen*, Liangbin Li*

National Synchrotron Radiation Lab & CAS Key Laboratory of Soft Matter Chemistry & Department of Polymer Science and Engineering, University of Science and Technology of China, Hefei, China.

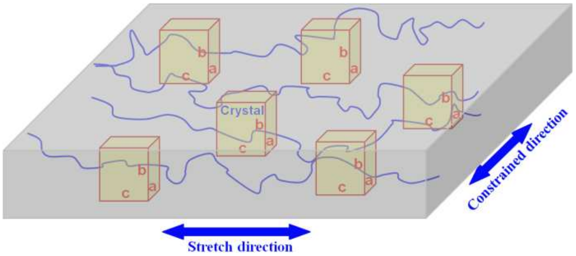

The single-crystal like orientation of natural rubber polycrystals are induced by constrained stretch, and the free energy of final state should be incorporate into the thermodynamic driving force for flow-induced crystallization.

---

[*] correspondence authors: rychen@ustc.edu.cn, lbli@ustc.edu.cn